



A Journal of the Gesellschaft Deutscher Chemiker

Angewandte Chemie

GDCh

International Edition

www.angewandte.org

Accepted Article

Title: Vacancy Engineering of Fe-doped W18O49 Nanoreactors for Low-barrier Electrochemical Nitrogen Reduction

Authors: Yueyu Tong, Haipeng Guo, Daolan Liu, Xiao Yan, Ji Liang, Panpan Su, Si Zhou, Jian Liu, Gao Qing (Max) Lu, and Shi Xue Dou

This manuscript has been accepted after peer review and appears as an Accepted Article online prior to editing, proofing, and formal publication of the final Version of Record (VoR). This work is currently citable by using the Digital Object Identifier (DOI) given below. The VoR will be published online in Early View as soon as possible and may be different to this Accepted Article as a result of editing. Readers should obtain the VoR from the journal website shown below when it is published to ensure accuracy of information. The authors are responsible for the content of this Accepted Article.

To be cited as: *Angew. Chem. Int. Ed.* 10.1002/anie.202002029
Angew. Chem. 10.1002/ange.202002029

Link to VoR: <http://dx.doi.org/10.1002/anie.202002029>
<http://dx.doi.org/10.1002/ange.202002029>

RESEARCH ARTICLE

Vacancy Engineering of Fe-doped $W_{18}O_{49}$ Nanoreactors for Low-barrier Electrochemical Nitrogen Reduction

Yueyu Tong, Haipeng Guo, Daolan Liu, Ji Liang*, Xiao Yan, Panpan Su, Si Zhou*, Jian Liu*, Gao Qing (Max) Lu and Shi Xue Dou

Y.Y. Tong, Dr. H.P. Guo, D.L. Liu, Dr. J. Liang, Dr. X. Yan, Dr. S. Zhou, Prof. S. X. Dou

Institute for Superconducting & Electronic Materials, Australian Institute of Innovative Materials, University of Wollongong, North Wollongong, NSW 2500, Australia
E-mail: liangj@uow.edu.au

A/Prof. P.P. Su, Prof. J. Liu

State Key Laboratory of Catalysis, Dalian Institute of Chemical Physics, Chinese Academy of Sciences, 457 Zhongshan Road, Dalian 116023, P. R. China

Prof. J. Liang

Key Laboratory for Advanced Ceramics and Machining Technology of Ministry of Education, School of Materials Science and Engineering, Tianjin University, Tianjin 300350, China

Dr. X. Yan

Guangdong Key Laboratory of Membrane Materials and Membrane Separation, Guangzhou Institute of Advanced Technology, Chinese Academy of Sciences, Guangzhou, 511458, China

Dr. S. Zhou

Key Laboratory of Materials Modification by Laser, Ion and Electron Beams (Dalian University of Technology), Ministry of Education, Dalian 116024, China

Email: siz@uow.edu.au

D.L. Liu, Prof. J. Liu, Prof. G. Q. Lu

DICP-Surrey Joint Centre for Future Materials, Department of Chemical and Process Engineering, and Advanced Technology Institute, University of Surrey, Guildford, Surrey, GU2 7XH, UK

E-mail: jian.liu@surrey.ac.uk; jianliu@dicp.ac.cn

Supporting information and the ORCID identification number(s) for the author(s) of this article can be found under <https://doi.org/>.

Abstract: Electrochemical nitrogen reduction reaction (NRR) is a promising energy-efficient and low-emission alternative to the traditional Haber-Bosch method. Usually, the competing hydrogen evolution reaction (HER) and reaction barrier of ambient electrochemical NRR are most significant challenges, making the simultaneous achievement of a high NH_3 yielding rate and a high Faradic efficiency (FE) extremely difficult for NRR. To address this issue, $W_{18}O_{49}$, with exposed W sites and intrinsically weak binding for H_2 , is doped by Fe to modify its surface atomic structure for effective NRR electrocatalysis and suppressed HER. On it, a high NH_3 yielding rate of $24.7 \mu g h^{-1} mg_{cat}^{-1}$ and a high FE of 20.0% have been simultaneously gained at a very low overpotential of $-0.15 V$ vs. reversible hydrogen electrode. *Ab initio* reveals an intercalation-type doping of Fe atoms in the tunnels of the $W_{18}O_{49}$ crystal structure, which increases the oxygen vacancies for exposing more W active sites, optimizes the nitrogen adsorption energy, and facilitates the electrocatalytic NRR. Thus, this work will provide a rational design of electrocatalysts for various electrochemical processes.

Introduction

Ammonia is an indispensable precursor for producing fertilizers, synthetic fibers, and pharmacies to satisfy the needs from the growing population and economy worldwide.^[1] More importantly, due to its high liquefied energy density and carbon-free nature, ammonia has also been regarded as an ideal storage intermediate for H_2 and a promising carbon-free fuel.^[2] Generally, the production of ammonia is associated with 1.44% of global CO_2 emission via the traditional Haber-Bosch process, which needs a high pressure of over 200 atm and a high temperature of over $500^\circ C$.^[3] Apart from this, the construction of the highly centralized

and large-scale Haber-Bosch plants is time, money, and space-consuming. In contrast, direct electroreduction of nitrogen to ammonia under ambient conditions, which was firstly demonstrated by Stoukides and coworkers,^[3a] presents a promising strategy to replace the traditional thermal catalysis process with reduced emission, lower energy consumption, and higher economic viability.^[4] However, the major bottleneck of electroreduction of nitrogen shifts to the competitive adsorption between hydrogen ions and nitrogen molecules in the aqueous environment and the activation of the ultra-stable $N\equiv N$ bond with a binding energy up to $940.95 kJ mol^{-1}$.^[5]

Addressing at this issue, various catalysts, especially the noble-metal-based ones, have been designed for the electrochemical nitrogen reduction reaction (NRR) under ambient conditions.^[6] However, their high costs and limited reserves largely impede the broad application of those noble-metal-based catalysts.^[7] Apart from the noble-metal catalysts, other delicately designed nanoreactors, in which the reactants could be enriched/preassembled and the intermediate processes/products could be stabilized, have also been studied.^[8a-b] However, the intrinsic hydrogen adsorption preference of these catalysts has greatly restrained their nitrogen adsorption capability, let alone the following electro-catalysis process.^[8c-d] Thus, exploring catalysts with a high selectivity for nitrogen adsorption is the prerequisite for achieving highly efficient NRR electrocatalysis with good economic feasibility for practical applications.

With this regard, a number of pioneering works have been conducted to overcome this difficulty, such as widening the potential gap between NRR and HER^[9] and designing active centers with intrinsic preference for nitrogen adsorption^[4a]. Although either a superior Faradic Efficiency (FE) or an outstanding ammonia yield rate has been achieved on these catalysts, to simultaneously achieve these two merits is still

RESEARCH ARTICLE

significantly challenging. Furthermore, reaching this goal at a low overpotential for a more energy-saving electrocatalytic NRR is even more challenging. This is, to some extent, resulted from the limited nitrogen adsorption sites, the sluggish NRR kinetics, and the dominating HER at high overpotentials.

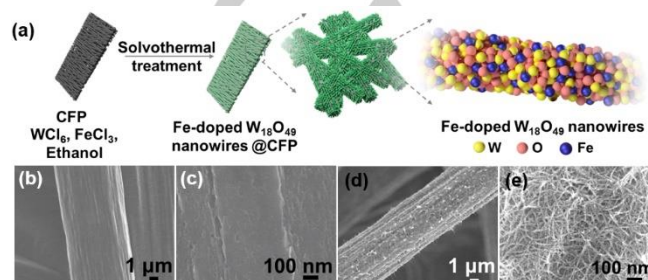
Considering this, defect-rich $W_{18}O_{49}$, the only nonstoichiometric oxide compositions of tungsten that can be isolated in a pure phase,^[10] might be an ideal candidate due to its intrinsically weak binding with hydrogen.^[11] In this case, however, the main challenge turns to be: (1) maximizing the exposure of possible active sites (*i.e.*, the W sites) and (2) the activation of N≡N to accelerate the sluggish NRR kinetics. For the former, the inherent oxygen vacancies (O_{vac}) in $W_{18}O_{49}$ have already laid a good foundation for disclosing more tungsten and facilitating the cleavage of nitrogen triple bond.^[12] While for the latter, surface chemical modification (*e.g.*, heteroatoms doping and/or defect engineering) has long been considered as a high-efficiency method for modulating the surface electronic structures of the electrochemical catalysts, which has been proven to be able to significantly enhance catalysts' activity for a range of applications, including oxygen reduction, oxygen evolution, hydrogen evolution, and nitrogen reduction.^[13]

For the defect-rich $W_{18}O_{49}$, the abundant tunnels in its lattice structure make it ideal for such modifications, which may generate enhanced NRR performance in return. Enlightened by the biological nitrogenase, iron (Fe) may enhance both the adsorption and activation of nitrogen molecules due to their strong interaction with nitrogen. In addition, as a transition metal element located in the middle part of the periodic table, the unoccupied d orbitals of Fe endow it both identities of electron-acceptor and electron-donor.^[14] More importantly, comparing to the d-spacing of $W_{18}O_{49}$ (3.8 Å), the relatively smaller radius of Fe atoms (1.2 Å) would greatly facilitate its intercalation into $W_{18}O_{49}$.^[15] Thus, the Fe-doping of $W_{18}O_{49}$ should not only modify its electronic structure but also tune the intrinsic covalency of its metal-oxygen bond, resulting in the refinement of the defect statement, improvement of the conductivity, and enhancement of N_2 adsorption capability.

Based on these considerations, we herein for the first time report a Fe-doped and defect-rich $W_{18}O_{49}$ nanowire, which is grown on carbon fiber papers (CFPs), as a freestanding and high-performance electrocatalyst for NRR. By simply changing the Fe-doping level, the defect status of $W_{18}O_{49}$ can be finely tuned, which results in the optimized nitrogen adsorption, suppressed hydrogen evolution, and enhanced charge transfer for electrocatalytic NRR. Due to these multi-synergetic effects, a greatly improved electrocatalytic NRR performance has been achieved. The $W_{18}O_{49}$ -16Fe @ CFP simultaneously acquires a high ammonia yield rate ($24.7 \mu\text{g h}^{-1} \text{mg}_{\text{cat}}^{-1}$) and a high FE of 20.0% at -0.15 V , which are much superior to those un-modified counterparts and most previous reported non-noble-metal catalysts. Especially, the quite low overpotential (-0.15 V) further improved the energy efficiency of electrocatalytic NRR, making it more energy-saving. *Ab initio* calculations further disclose that it is the Fe atoms, which are intercalated in the tunnels of $W_{18}O_{49}$, that lead to the redistribution surface electrons of $W_{18}O_{49}$ to substantially promote its N_2 fixation ability and minimize the NRR overpotentials. Thus, our work will blaze a new trial for both the rational design of catalysts and the elaborate clarification of mechanism for NRR at ambient conditions.

Results and Discussion

The solvothermal fabrication of the material is illustrated in **Figure 1a, S1**. By tuning the ratio of WCl_6 and $FeCl_3$, the doping level in the obtained $W_{18}O_{49}$ can be tuned (denoted as $W_{18}O_{49}$ -xFe @ CFPs, x=4, 8, 16, 32, x was the designed mole percentage of Fe). Fe-doped $W_{18}O_{49}$ without CPF was also prepared. The color of $W_{18}O_{49}$ changes from navy blue to grey green and finally to brown with Fe content increasing, clearly suggesting the successful doping of Fe in $W_{18}O_{49}$ by this process (**Figure S2**). Details about the fabrication process can be found in the



supplementary information.

Figure 1. (a) Schematic illustration of the preparation of Fe-doped $W_{18}O_{49}$ nanowires @ CFP. SEM images of (b-c) CFP, (d-e) $W_{18}O_{49}$ -16Fe nanowires @ CFP.

After the formation of $W_{18}O_{49}$, a large number of thorn-like structures can be observed on the surface of CFP, which is originally smooth (**Figure 1b, c**). High magnification images further show those thorn-like structures are nanowires with a length of several micrometers, homogeneously tangling on the CFP (**Figure 1d, e**). With the variation of the designed Fe-doping concentration from 0 to 32%, the thorn-like structure on CFP gradually aggregates, but the homogeneous nanowires still remain (**Figure S3a-h**). This is in good agreement with the transmission electron microscopy (TEM) observation, which also reveals the homogeneous nanowire architecture of Fe-doped $W_{18}O_{49}$ (**Figure 2a, S3i-l**). Besides, the select-area electron diffraction (SAED) patterns of the nanowires also confirm their crystalline nature along the (010) direction, regardless of the Fe-doping level (**Figure 2b inset and S3i-l**), indicating the Fe-doping does not change the crystal structure of the $W_{18}O_{49}$ host, which is beneficial for the stable NRR electrocatalysis.

The microstructure of these Fe-doped $W_{18}O_{49}$ nanowires was then studied using high-angle annular dark-field scanning transmission electron microscope (HAADF-STEM). These nanowires, with diameters of less than 5 nm, clearly show lattice fringes of $\sim 0.38 \text{ nm}$, which belong to (010) planes of $W_{18}O_{49}$ and further verifies their preference growth along the [010] direction (**Figure 2b, S3m-p**). Notably, Fe-doping does not induce obvious change of the lattice parameter of $W_{18}O_{49}$ according to both SAED and HAADF-STEM measurements, indicating the robustness of $W_{18}O_{49}$ structures upon Fe-doping. The XRD patterns of the Fe-doped $W_{18}O_{49}$ nanowires, which were scraped off from CFP, show monoclinic $W_{18}O_{49}$ phase, with characteristic peaks at around 23°

RESEARCH ARTICLE

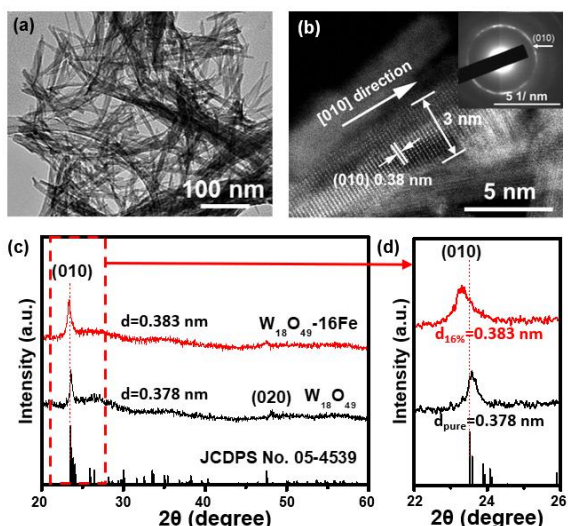


Figure 2. (a) TEM image, (b) HAADF-STEM images of $W_{18}O_{49}$ -16Fe nanowires @ CFP. Insert is the corresponding SAED pattern. (c) XRD patterns of $W_{18}O_{49}$ -16Fe nanowires and pure $W_{18}O_{49}$ nanowires. (d) enlarged XRD patterns of $W_{18}O_{49}$ -16Fe nanowires and pure $W_{18}O_{49}$ nanowires in the $2\theta=22^{\circ}$ - 26° region.

and 47° that can be ascribed to (010) and (020) facets (JCPDS No. 05-4539, Figure 2c-d and S4), respectively. Interestingly, with increasing Fe-doping level from 0 to 32%, a small shift of the (010) peak towards a lower degree can be observed (Figure 2d, S4b-c, and Table S1), indicating the very slight expansion of the monoclinic structure of $W_{18}O_{49}$ due to the Fe-doping, which will be discussed later (Figure S5).

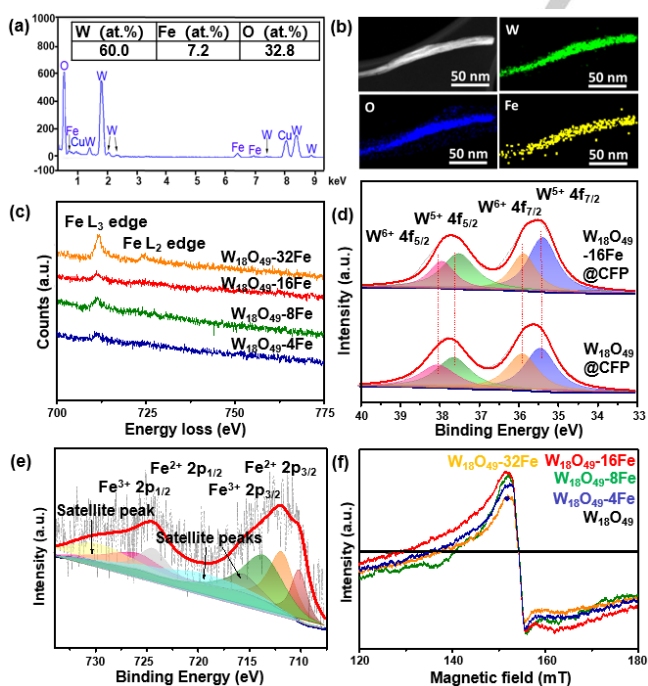


Figure 3. (a-b) EDS spectrum and STEM-EDS images of $W_{18}O_{49}$ -16Fe nanowires. (c) Fe- $L_{2,3}$ spectra of as-prepared Fe-doped $W_{18}O_{49}$ nanowires. High-resolution (d) W 4f and (e) Fe 2p XPS spectra of $W_{18}O_{49}$ -16Fe nanowires @ CFP. (f) EPR spectra of all Fe-doped $W_{18}O_{49}$ nanowires and pure $W_{18}O_{49}$ nanowires at $-150^{\circ}C$.

To further confirm the successful doping of Fe element into $W_{18}O_{49}$, energy dispersion spectrum (EDS)-based elemental mappings and Fe- $L_{2,3}$ edge EELS spectra of the doped nanowires were obtained (Figure 3a-c, S6), which show homogeneous distributions of W, O, and Fe without any other elements detected. With the increasing amount of $FeCl_3$ in the precursor, the Fe content in the doped $W_{18}O_{49}$ nanowires also increases, as confirmed by both EDS and XPS results (Table S2). The Fe/W ratio acquired from HAADF-STEM-EDS is quite close to that in the $FeCl_3$ and WCl_6 precursors, indicating that the Fe-doping concentration in $W_{18}O_{49}$ can be precisely controlled. On the other hand, the Fe/W ratio derived from XPS spectra is much higher than the EDS results, which implies that the Fe dopants mostly exist in the near-surface region of $W_{18}O_{49}$ nanowires, more efficient for the surface modification to participate in the NRR electrocatalysis.

X-ray photoelectron spectroscopy (XPS) was then applied to further identify the chemical states of the elements in the synthesized samples. The XPS survey scan confirms the presence of W, Fe, O, and C elements in all the Fe-doped $W_{18}O_{49}$ @ CFP analogues (Figure S7a). The deconvoluted high-resolution W 4f spectra of pristine and $W_{18}O_{49}$ -16Fe nanowires suggests both W^{5+} and W^{6+} species present in the samples (Figure 3d, Figure S7b), which is consistent with the distorted edge-sharing crystal structure of $W_{18}O_{49}$ forming low-valence W elements and metallic W-W interaction in the lattice.^[16] Compared with the pristine $W_{18}O_{49}$, the $W_{18}O_{49}$ -16Fe showed an increased W^{5+}/W^{6+} ratio from 1.2 to 1.7 and a clear shift to the lower binding energy (Table S3), indicating the partial reduction of W^{6+} into W^{5+} associated with the increase of O_{vac} .^[11, 17] On the other hand, for the Fe 2p spectra, it can be deconvoluted into four peaks at around 710.5, 712.3, 723.8 and 725.6 eV (Figure 3e, Figure S7c), corresponding to the $Fe^{2+} 2p_{3/2}$, $Fe^{3+} 2p_{3/2}$, $Fe^{2+} 2p_{1/2}$, and $Fe^{3+} 2p_{1/2}$ states, respectively.^[17-18] Besides, the additional pre-peak in the low-binding-energy region (708.7 eV) accounts for the Fe ions with a lower oxidation state than Fe^{2+} , further revealing the existence of O_{vac} in the neighboring sites of Fe dopants.^[18]

Electron paramagnetic resonance (EPR) spectroscopy was used to investigate the unpaired electrons in the synthesized samples, the amount of which is proportional to the O_{vac} content (Figure 3f). Compared with the pure $W_{18}O_{49}$, the increased EPR intensity (i.e., a higher unpaired electron/ O_{vac} content) of the Fe-doped counterparts can be attributed to Fe atoms located next to the charge-compensating oxygen vacancies, resulting in the lower-oxidation-state of Fe atoms.^[17, 19] The highest EPR intensity of $W_{18}O_{49}$ means the most intense charge-compensating effect, indicating the highest concentration of O_{vac} in it, which is essential to generate more active sites for NRR catalysis as will be discussed later (Figure 3f). Moreover, the absent signal of free electrons in the region of mT > 180 indicates that electrons tend to be captured by Fe ions rather than delocalization within the lattice of $W_{18}O_{49}$, suggesting an 'electron reservoir' role of the Fe dopants.^[20] This 'electron reservoir' is believed to be of great benefit for the hydrogenation of nitrogen during the ammonia production process.

The ambient electrocatalytic NRR performance of the as-prepared samples was investigated in a N_2 -saturated 0.25 M $LiClO_4$ aqueous solution and the ammonia yield was determined by the salicylic acid method (Figure S8, S9-S13). In general, the ammonia yield rate and FE for all the Fe doped- $W_{18}O_{49}$ @ CFP catalysts gradually increase with the negative shift of testing

RESEARCH ARTICLE

potential till the peak value during the NRR tests. After that, decrease in FE and NH_3 yield rate occur due to the hydrogen adsorption surpassing the nitrogen adsorption on the surface of catalysts.^[9] Among them, the 16% Fe-doped one showed both the largest NH_3 yield rate of $24.7 \mu\text{g h}^{-1} \text{mg}_{\text{cat}}^{-1}$ and the highest FE of 20.0% at -0.15 V vs. RHE , which are 12 times and 2 times higher than the pristine $\text{W}_{18}\text{O}_{49}$ @ CFP catalyst, respectively (Figure 4a-b). Remarkably, overpotential of -0.15 V is much lower than the values of most reported electrocatalysts for NRR by far,^[4a, 7a, 7b, 21] and at this overpotential, the $\text{W}_{18}\text{O}_{49}$ -16Fe @ CFP simultaneously achieves the highest ammonia yield rate and FE with neither feature sacrificed (Table S4). As the Fe-doping concentration further increased to 32%, the ammonia yield rate and FE significantly dropped to $1.72 \mu\text{g h}^{-1} \text{mg}_{\text{cat}}^{-1}$ and 7.6%, which indicates the optimized electrocatalytic performance of $\text{W}_{18}\text{O}_{49}$ at an appropriate Fe doping level. The selective NH_3 production against hydrazine of all the Fe-doped $\text{W}_{18}\text{O}_{49}$ @ CFP samples were also evaluated by the Watt and Chrisp methods (Figure S14, S15), and no hydrazine was detected (Figure S15), which further demonstrates the excellent selectivity of the as-prepared catalysts.

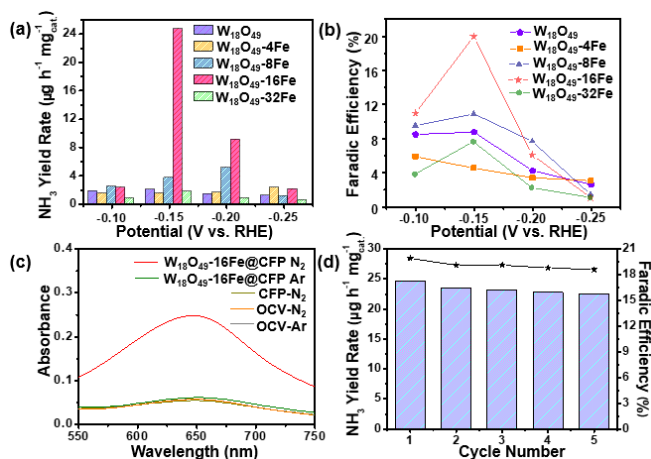


Figure 4. (a) NH_3 yield rate at various potentials vs. RHE. (b) Faradic efficiency of as-prepared Fe-doped $\text{W}_{18}\text{O}_{49}$ nanowires @ CFP electrodes. (c) UV-vis absorption spectra of various electrolytes stained with salicylic acid indicator. OCV stands for open-circuit voltage. (d) cycling stability results at -0.15 V vs. RHE of $\text{W}_{18}\text{O}_{49}$ -16Fe nanowires @ CFP electrode.

The origin of the produced ammonia was then verified to eliminate any possible interference from contaminants (Figure 4c). Specifically, when the catalyst was placed in the electrolyte at open-circuit voltages (OCVs) for 10 h, no ammonia could be detected in either N_2 - or Ar-saturated electrolytes, confirming no ammonia contamination from the gases or the catalysts used in this work. When N_2 was replaced by Ar for NRR electrocatalysis over the samples, no apparent ammonia production was detected, proving that the ammonia is produced from the feeding N_2 (Figure S16). Moreover, when a bare CFP was used as the catalytic electrode, no apparent ammonia production was detected either, further confirming that the ammonia was produced from the NRR electrocatalysis over the Fe-doped $\text{W}_{18}\text{O}_{49}$, rather than from the CFP electrocatalysis. On this basis, it is evidenced that the excellent ammonia yield rate and FE are due to the NRR electrocatalysis over the $\text{W}_{18}\text{O}_{49}$ -16Fe @ CFP catalyst.

Apart from the NRR activity, the durability is another critical quality for electrocatalysts. For the $\text{W}_{18}\text{O}_{49}$ -16Fe @ CFP material, a high ammonia yield rate retention up to 91% was obtained after five continuous electrolysis cycles without any obvious decay in its efficiency, clearly demonstrating its excellent stability for NRR electrocatalysis (Figure 4d, S17a, b). Furthermore, the very stable NRR current over 20 h for the catalyst also verifies its superior electrocatalytic durability (Figure S17c). This stable electrochemical behavior also agrees well with intact microstructure of the catalyst after the long-term test (Figure S18). Little changes were observed in the XPS spectrum of $\text{W}_{18}\text{O}_{49}$ -16Fe @ CFP catalyst after the durability test, further verifying its excellent stability for NRR electrocatalysis in aqueous solution. (Figure S19).

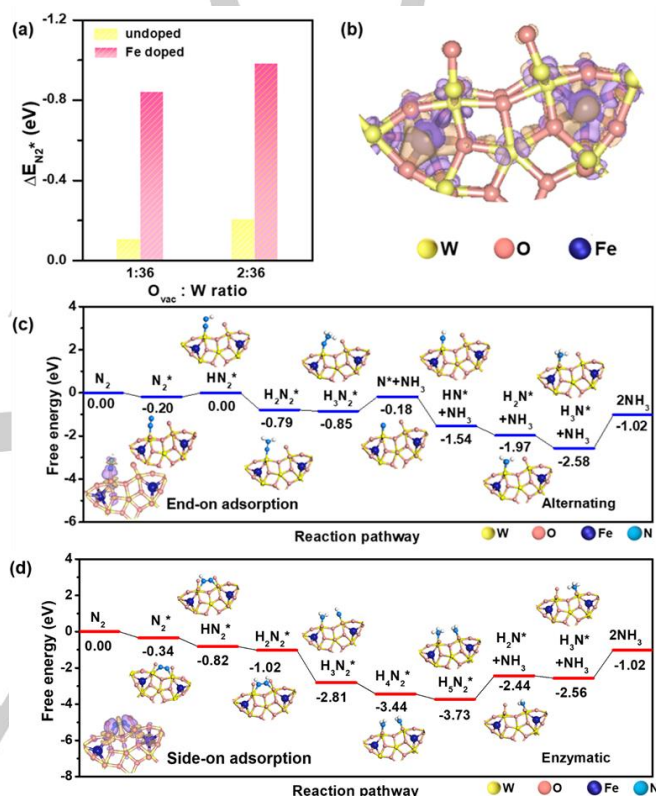


Figure 5. (a) N_2 adsorption energy (ΔE_{N_2}) as a function of $\text{O}_{\text{vac}} : \text{W}$ ratio for $\text{W}_{18}\text{O}_{49}$ with and without Fe doping by DFT calculations. (b) The differential charge density between Fe and $\text{W}_{18}\text{O}_{49}$ with $\text{O}_{\text{vac}} : \text{W}$ ratio of 2 : 36 without N_2 chemisorption. Purple and orange colors represent electron accumulation and depletion regions, respectively, with isosurface value of $5 \times 10^{-3} \text{ e}\text{\AA}^{-3}$. (c, d) Free energy diagrams of NRR on Fe-doped $\text{W}_{18}\text{O}_{49}$ with $\text{O}_{\text{vac}} : \text{W}$ ratio of 1 : 36 and 2 : 36, respectively. The structures of reaction intermediates are shown next to their energy segments. Left bottom of (c, d) inserted the differential charge density distributions of N_2 chemisorbed on Fe-doped $\text{W}_{18}\text{O}_{49}$ with $\text{O}_{\text{vac}} : \text{W}$ ratio of 1 : 36 and 2 : 36, respectively. The Fe/W ratio is fixed at 11%.

To better understand the roles of Fe-doping and O_{vac} on the electrocatalytic NRR activity of $\text{W}_{18}\text{O}_{49}$, DFT calculations were carried out. A slab model of $\text{W}_{18}\text{O}_{49}$ (100) surface was adopted based on the HAADF-STEM results, with different numbers of O_{vac} being considered. As $\text{W}_{18}\text{O}_{49}$ possesses pore-like channels, Fe atoms might either intercalate into the channel or substitute the W atoms. Our calculations show that intercalation of Fe atom into the $\text{W}_{18}\text{O}_{49}$ channel is both energetically and kinetically favorable, with a low kinetic barrier of 0.37 eV and heat of

RESEARCH ARTICLE

formation of 1.43 eV (Figure S20). Intercalation at the Fe/W ratio of 11% (close to the EDS tested experimental doping concentration 12%) leads to slight expansion of lattice parameters of $W_{18}O_{49}$ below 1% (Figure S21a), which is consistent with the TEM and XRD observations (Figure 2b, c). Therefore, it is reasonable to deduce that the Fe dopants are most probably intercalated in the channels of $W_{18}O_{49}$, which has also been reported in the previous works.^[15a, 22]

Such Fe intercalation can remarkably enhance the binding capability of the W atoms in $W_{18}O_{49}$ to N_2 molecules (Figure 5a). For the undoped $W_{18}O_{49}$ with different designed levels of O_{vac} , only very small adsorption energies ($\Delta E_{N_2^*}$, relative to free N_2) of -0.10 to 0.20 eV can be achieved, which means N_2 molecule can only be very weakly adsorbed on their surface. In contrast, when Fe atoms are doped on them, the N_2 adsorption strength is remarkably enhanced with $\Delta E_{N_2^*}$ of -0.84 to -0.99 eV. Moreover, when adsorbed on the Fe-doped $W_{18}O_{49}$, the $N=N$ bond length of the N_2 molecules can also be significantly elongated from 1.10 Å for free N_2 molecule to 1.25 Å, suggesting the successful activation of N_2 molecule and high surface activity of the material (Figure S21b-c). Note that we also considered substitutional doping of Fe into $W_{18}O_{49}$, which, however, greatly weakens the binding capability of $W_{18}O_{49}$ with N_2 with regard to the pristine system (Figure S22), and contradict the observed enhanced activity of Fe-doped $W_{18}O_{49}$ in experiment.

The full reaction pathways of NRR over the Fe-doped $W_{18}O_{49}$ with different O_{vac} levels were then explored (Figure 5c, d). At a low O_{vac} level (i.e., $O_{vac}/W = 1/36$) with fewer W sites exposed, on which N_2 can only be adsorbed at the W sites with the end-on configuration, NRR occurs via the alternating pathway, involving a small potential step of 0.20 eV during the formation of HN_2^* species. At a higher O_{vac} level, N_2 molecules favor the side-on adsorption and NRR proceeds through the enzymatic pathway. In this case, the whole reaction is almost barrierless except for the desorption of NH_3 , in good accord with the extremely low overpotential measured in experiment. Meanwhile, HER is also largely inhibited due to the weaker binding of H^* species on the W sites in comparison with N_2 (the adsorption strength of H^* is 0.60 eV less than that for N_2). Therefore, the Fe-doping and presence of oxygen vacancies in $W_{18}O_{49}$ both contribute to the enhanced N_2 fixation and favorable reduction.

Deeper insights can be obtained from the differential charge density distributions and electronic density of states (DOS) presented in Figure 5b, left bottom illustrations in Figure 5c, d, and Figure S23, respectively. Prominent electron transfer occurs from Fe atoms to $W_{18}O_{49}$ (Figure 5b, left bottom illustrations in Figure 5c, d). According to the Bader charge analysis, each W atom gains 0.04 e from Fe dopant, and thus exhibits enhanced binding capability with N_2 compared to that of the pristine $W_{18}O_{49}$. Moreover, the electronic states induced by Fe-doping fill the original gap of $W_{18}O_{49}$ at around -1.0 eV in the DOS (Figure S23), which may be beneficial to improve the electronic conductivity during NRR. On the other aspect, the presence of O_{vac} not only helps expose more W active centers for NRR, but also affects the work function of $W_{18}O_{49}$. A higher O_{vac} level leads to the reduction of work function and the approaching of $W_{18}O_{49}$'s Fermi level towards the π^* state of N_2 molecule (-1.89 eV relative to vacuum), which will facilitate the backdonation of electrons from $W_{18}O_{49}$ to N_2 for NRR. Consequently, these two factors synergistically contribute to the enhanced NRR activity for the Fe-doped $W_{18}O_{49}$ nanowires.

Conclusion

In summary, Fe-doped $W_{18}O_{49}$ nanowires have been successfully fabricated on carbon fiber papers, through a facile hydrothermal method, for high-performance electrocatalysis of NRR. The $W_{18}O_{49}$ -16Fe @ CFP nanoreactor achieved the highest electrocatalytic NRR performance, in terms of a high ammonia yield rate of $24.7 \mu\text{g h}^{-1} \text{mg}_{\text{cat}}^{-1}$ and high Faradic efficiency of 20.0% at a very low over potential of -0.15 V vs. RHE. Our experimental characterization combined with DFT calculations reveal that it is the Fe intercalation strategy and the modified O_{vac} state that simultaneously optimizes the electronic states and surface properties of $W_{18}O_{49}$, leading to the enhanced binding capability for nitrogen fixation-more active sites, the higher electrical conductivity, the better nitrogen adsorption strength, and the low-barrier NRR pathway. Thus, this work not only provides an outstanding electrocatalyst for NRR, but also, more importantly, opens a new avenue for modulating the electronic and catalytic properties of nanoreactors for various electrochemical processes.

Acknowledgements

Dr. X. Yan thanks China Scholarship Council for supporting his visit to the University of Wollongong (No. 201804910018). This work was supported by NCI supercomputer resources, National Natural Science Foundation of China (No. 51502045 and 21905202), Dalian National Laboratory for Clean Energy (DNL), CAS, DNL Cooperation Fund, CAS (DNL180402), and Australian Research Council (ARC) through Discovery Early Career Researcher Award (DECRA, No. DE170100871).

Keywords: Vacancy engineering • nitrogen reduction reaction • electrocatalysts • tungsten oxide • nanoreactor

- [1] a) I. Ćorić, B. Q. Mercado, E. Bill, D. J. Vinyard, P. L. Holland, *Nature* **2015**, *526*, 96; b) T. Spatzal, K. A. Perez, O. Einsle, J. B. Howard, D. C. Rees, *Science* **2014**, *345*, 1620-1623; c) G.-F. Chen, S. Ren, L. Zhang, H. Cheng, Y. Luo, K. Zhu, L.-X. Ding, H. Wang, *Small Methods* **2019**, *3*, 1800337.
- [2] a) V. Rosca, M. Duca, M. T. de Groot, M. T. M. Koper, *Chem. Rev.* **2009**, *109*, 2209-2244; b) S. Licht, B. Cui, B. Wang, F.-F. Li, J. Lau, S. Liu, *Science* **2014**, *345*, 637-640; c) A. Klerke, C. H. Christensen, J. K. Nørskov, T. Vegge, *J. Mater. Chem.* **2008**, *18*, 2304-2310.
- [3] a) G. Soloveichik, *Nat. Catal.* **2019**, *2*, 377-380; b) B. H. R. Suryanto, H.-L. Du, D. Wang, J. Chen, A. N. Simonov, D. R. MacFarlane, *Nat. Catal.* **2019**, *2*, 290-296.
- [4] a) Y. Wang, M.-M. Shi, D. Bao, F.-L. Meng, Q. Zhang, Y.-T. Zhou, K.-H. Liu, Y. Zhang, J.-Z. Wang, Z.-W. Chen, D.-P. Liu, Z. Jiang, M. Luo, L. Gu, Q.-H. Zhang, X.-Z. Cao, Y. Yao, M.-H. Shao, Y. Zhang, X.-B. Zhang, J. G. Chen, J.-M. Yan, Q. Jiang, *Angew. Chem., Int. Ed.* **2019**, *58*, 9464-9469; b) J. G. Chen, R. M. Crooks, L. C. Seefeldt, K. L. Bren, R. M. Bullock, M. Y. Darensbourg, P. L. Holland, B. Hoffman, M. J. Janik, A. K. Jones, M. G. Kanatzidis, P. King, K. M. Lancaster, S. V. Lymar, P. Pfromm, W. F. Schneider, R. R. Schrock, *Science* **2018**, *360*, eaar6611.
- [5] D. Bao, Q. Zhang, F.-L. Meng, H.-X. Zhong, M.-M. Shi, Y. Zhang, J.-M. Yan, Q. Jiang, X.-B. Zhang, *Adv. Mater.* **2017**, *29*, 1604799.
- [6] X. Yan, D. Liu, H. Cao, F. Hou, J. Liang, S. X. Dou, *Small Methods* **2019**, *3*, 1800501.
- [7] a) M.-M. Shi, D. Bao, S.-J. Li, B.-R. Wulan, J.-M. Yan, Q. Jiang, *Adv. Energy Mater.* **2018**, *8*, 1800124; b) H. Tao, C. Choi, L.-X. Ding, Z. Jiang, Z. Han, M. Jia, Q. Fan, Y. Gao, H. Wang, A. W. Robertson, S. Hong, Y. Jung, S. Liu, Z. Sun, *Chem* **2019**, *5*, 204-214; c) M.-M. Shi, D. Bao, B.-R. Wulan, Y.-H. Li, Y.-F.

RESEARCH ARTICLE

- Zhang, J.-M. Yan, Q. Jiang, *Adv. Mater.* **2017**, *29*, 1606550; d) J. Wang, L. Yu, L. Hu, G. Chen, H. Xin, X. Feng, *Nat. Commun.* **2018**, *9*, 1795.
- [8] a) H. Tian, J. Liang, J. Liu, *Adv. Mater.* **2019**, *31*, 1903886; b) Y.-Y. Tong, X. Yan, J. Liang, S. X. Dou, *Small* **2019**, 1904126; c) C. Guo, J. Ran, A. Vasileff, S.-Z. Qiao, *Energy Environ. Sci.* **2018**, *11*, 45-56; d) J. K. Nørskov, T. Bligaard, A. Logadottir, J. R. Kitchin, J. G. Chen, S. Pandelov, U. Stimming, *J. Electrochem. Soc.* **2005**, *152*, J23-J26.
- [9] M. Wang, S. Liu, T. Qian, J. Liu, J. Zhou, H. Ji, J. Xiong, J. Zhong, C. Yan, *Nat. Commun.* **2019**, *10*, 341.
- [10] C. Guo, S. Yin, M. Yan, M. Kobayashi, M. Kakihana, T. Sato, *Inorganic Chemistry* **2012**, *51*, 4763-4771.
- [11] X. Zhong, Y. Sun, X. Chen, G. Zhuang, X. Li, J.-G. Wang, *Adv. Funct. Mater.* **2016**, *26*, 5778-5786.
- [12] a) Y. Zhao, Y. Zhao, G. I. N. Waterhouse, L. Zheng, X. Cao, F. Teng, L.-Z. Wu, C.-H. Tung, D. O'Hare, T. Zhang, *Adv. Mater.* **2017**, *29*, 1703828; b) H. Li, J. Shang, Z. Ai, L. Zhang, *J. Am. Chem. Soc.* **2015**, *137*, 6393-6399.
- [13] a) Q. Wang, Y. Lei, D. Wang, Y. Li, *Energy Environ. Sci.* **2019**, *12*, 1730-1750; b) S. Wang, F. Ichihara, H. Pang, H. Chen, J. Ye, *Adv. Funct. Mater.* **2018**, *28*, 1803309; c) D. Yan, H. Li, C. Chen, Y. Zou, S. Wang, *Small Methods* **2019**, *3*, 1800331.
- [14] C. Ling, Y. Ouyang, Q. Li, X. Bai, X. Mao, A. Du, J. Wang, *Small Methods* **2019**, *3*, 1800376.
- [15] a) M. R. Thalji, G. A. M. Ali, H. Algarni, K. F. Chong, *J. Power Sources* **2019**, *438*, 227028; b) L.-J. Guo, G.-F. Zhao, Y.-Z. Gu, X. Liu, Z. Zeng, *Phys. Rev. B* **2008**, *77*, 195417.
- [16] N. Zhang, A. Jalil, D. Wu, S. Chen, Y. Liu, C. Gao, W. Ye, Z. Qi, H. Ju, C. Wang, X. Wu, L. Song, J. Zhu, Y. Xiong, *J. Am. Chem. Soc.* **2018**, *140*, 9434-9443.
- [17] T. Wu, Z. Xing, S. Mou, C. Li, Y. Qiao, Q. Liu, X. Zhu, Y. Luo, X. Shi, Y. Zhang, X. Sun, *Angew. Chem., Int. Ed.* **2019**, *58*, 18449.
- [18] A. P. Grosvenor, B. A. Kobe, M. C. Biesinger, N. S. McIntyre, *Surf. Interface Anal.* **2004**, *36*, 1564-1574.
- [19] W. Zhao, J. Zhang, X. Zhu, M. Zhang, J. Tang, M. Tan, Y. Wang, *Appl. Catal., B* **2014**, *144*, 468-477.
- [20] Z. Ying, S. Chen, S. Zhang, T. Peng, R. Li, *Appl. Catal., B* **2019**, *254*, 351-359.
- [21] a) L. Li, C. Tang, B. Xia, H. Jin, Y. Zheng, S.-Z. Qiao, *ACS Catal.* **2019**, *9*, 2902-2908; b) Y. Zhang, W. Qiu, Y. Ma, Y. Luo, Z. Tian, G. Cui, F. Xie, L. Chen, T. Li, X. Sun, *ACS Catal.* **2018**, *8*, 8540-8544; c) Y. Fang, Z. Liu, J. Han, Z. Jin, Y. Han, F. Wang, Y. Niu, Y. Wu, Y. Xu, *Adv. Energy Mater.* **2019**, *9*, 1803406; d) X. Li, T. Li, Y. Ma, Q. Wei, W. Qiu, H. Guo, X. Shi, P. Zhang, A. M. Asiri, L. Chen, B. Tang, X. Sun, *Adv. Energy Mater.* **2018**, *8*, 1801357; e) H. Cheng, L.-X. Ding, G.-F. Chen, L. Zhang, J. Xue, H. Wang, *Adv. Mater.* **2018**, *30*, 1803694; f) C. Lv, C. Yan, G. Chen, Y. Ding, J. Sun, Y. Zhou, G. Yu, *Angew. Chem., Int. Ed.* **2018**, *57*, 6073-6076; g) D. Wu, H. Wang, H. Huang, R. Zhang, L. Ji, H. Chen, Y. Luo, J. You, D. Tang, Z. Zhang, X. Sun, *Chem. Commun.* **2019**, *55*, 7546-7549; h) Y. Luo, G.-F. Chen, L. Ding, X. Chen, L.-X. Ding, H. Wang, *Joule* **2019**, *3*, 279-289; i) H.-M. Liu, S.-H. Han, Y. Zhao, Y.-Y. Zhu, X.-L. Tian, J.-H. Zeng, J.-X. Jiang, B. Y. Xia, Y. Chen, *J. Mater. Chem. A* **2018**, *6*, 3211-3217; j) J. Lv, S. Wu, Z. Tian, Y. Ye, J. Liu, C. Liang, *J. Mater. Chem. A* **2019**, *7*, 12627-12634; k) X. Zhang, Q. Liu, X. Shi, A. M. Asiri, Y. Luo, X. Sun, T. Li, *J. Mater. Chem. A* **2018**, *6*, 17303-17306; l) J. Zhao, L. Zhang, X.-Y. Xie, X. Li, Y. Ma, Q. Liu, W.-H. Fang, X. Shi, G. Cui, X. Sun, *J. Mater. Chem. A* **2018**, *6*, 24031-24035; m) W. Fu, Y. Cao, Q. Feng, W. R. Smith, P. Dong, M. Ye, J. Shen, *Nanoscale* **2019**, *11*, 1379-1385; n) H. Wang, H. Yu, Z. Wang, Y. Li, Y. Xu, X. Li, H. Xue, L. Wang, *Small* **2019**, *15*, 1804769; o) X. Wu, L. Xia, Y. Wang, W. Lu, Q. Liu, X. Shi, X. Sun, *Small* **2018**, *14*, 1803111; p) W. Guo, Z. Liang, J. Zhao, B. Zhu, K. Cai, R. Zou, Q. Xu, *Small Methods* **2018**, *2*, 1800204; q) J.-X. Yao, D. Bao, Q. Zhang, M.-M. Shi, Y. Wang, R. Gao, J.-M. Yan, Q. Jiang, *Small Methods* **2019**, *3*, 1800333.
- [22] A. Martínez-de la Cruz, U. Amador, J. Rodríguez-Carvajal, F. García-Alvarado, *J. Solid State Chem.* **2005**, *178*, 2998-3003.

RESEARCH ARTICLE

Entry for the Table of Contents



Efficient electrochemical Nitrogen reduction reaction (NRR): Both High NH_3 yielding rate ($24.7 \mu\text{g h}^{-1} \text{mg}_{\text{cat}}^{-1}$) and Faradic efficiency (20.0%) achieving on the nanoreactor of Fe doped $\text{W}_{18}\text{O}_{49}$ nanowires @ carbon fiber papers at -0.15 V vs. reversible hydrogen electrode. Fe atoms not only efficiently increase oxygen vacancies of $\text{W}_{18}\text{O}_{49}$, but optimize the nitrogen adsorption energy, and facilitates the electrocatalytic NRR.